Electrodeformation of vesicles suspended in a liquid medium

Adnan Morshed,[1] Prashanta Dutta,[1,*] Mohammad Robiul Hossan,[2] and Robert Dillon[3]

[1]*School of Mechanical and Materials Engineering, Washington State University, Pullman, Washington 99164, USA*

[2]*Department of Engineering and Physics, University of Central Oklahoma, Edmond, Oklahoma 73034, USA*

[3]*Department of Mathematics and Statistics, Washington State University, Pullman, Washington 99164, USA*

Deformation of flexible vesicles suspended in a fluid medium due to an applied electric field can provide valuable insight into deformation dynamics at a very small scale. In an electric field, the response of the vesicle membrane is strongly influenced by the conductivity of surrounding fluid, vesicle size, and shape, and the magnitude of applied field. We studied the electrodeformation of vesicles immersed in a fluid media under a dc electric field. An immersed interface method is used to solve the electric field over the domain with conductive or nonconductive vesicles while an immersed boundary method is employed to solve fluid flow, fluid-solid interaction, membrane mechanics, and vesicle deformation. Initial force analysis on the membrane surface reveals almost linear influence of vesicle size, but the vesicle size does not affect the long-term deformation which is consistent with experimental evidence. Highly nonlinear effects of the applied field as well as the conductivity ratios inside and outside of the vesicle are observed. Results also point toward an early linear deformation regime followed by an equilibrium stage for the membranes. Modeling results suggest that electrodeforming vesicles can create unique external flows for different conductivity ratios. Moreover, significant influence of the initial aspect ratio of the vesicle on the force distribution is observed across a range of conductivity ratios.

I. INTRODUCTION

Biological cell manipulation, cellular nutrient transport, and drug delivery are some of the most intensive topics in biophysical research. In each of these emerging research areas, biovesicles are playing a fundamental role. Their functions are as varied as their size. For example, HIV-1 infected cells release nanoscale extracellular vesicles (exosomes) that mediate virus attachment and fusion to target cells [1]. At the same time, a host of biomimetic vesicles can be engineered as nanoscale drug carriers to target inflamed tissues [2,3]. Another important example is the endosomal vesicles which continuously perform innumerable intracellular tasks in cellular endocytosis and exocytosis. At the microscale, most eukaryotic cells themselves are yet another example of large biological vesicles (aka giant vesicle). Prediction of the adaptive response of each of these vesicles in a given environment requires the understanding of their behavior. More specifically, critical understanding of their dynamics is needed for proper manipulation in a specific targeted application like drug delivery. One promising approach is the study of lipid membrane or cell deformation through interaction with electric fields.

---

*Corresponding author: prashanta@wsu.edu

Application of an electric field on microparticles, such as vesicles, bubbles, and beads suspended in a liquid medium results in altered kinetics, electro-osmotic flow, and electrodeformation. Depending on the surface charge, geometry, and electrical properties, different vesicles produce varying levels of response. These responses include rotation, translation, assembly and orientation [4], deformation, and electroporation and fusion [5]. Both alternating current (ac) and direct current (dc) fields are being actively employed in tissue ablation, cell deformation, and characterization of the mechanical properties of lipid vesicles [6,7]. Application of dc fields facilitates the investigation of vesicle transport as well as electrodeformation [8], while ac fields allow for observation of a wide range of membrane mechanics using electric field magnitude and frequency as control parameters [9]. In biomedical and biotechnology applications, electrodeformation has been extensively used for studying mechanics of cell and label-free microfluidic characterization. For example, electrode-formation has been used to characterize TGF-β–dependent epithelial to mesenchymal transition of cancer cells [10]. It has also been successfully employed to separate malaria-infected red blood cells from healthy ones in a microfluidic device [11]. Engineered giant lipid vesicles (generally a few tens of micrometers in diameter) are another major avenue under study with electric fields due to their close resemblance to biological cells [12]. The size of both naturally occurring and engineered vesicles can range from nanometers to tens of microns. Giant vesicles have been predominantly used for the measurement of rheological and mechanical properties of the membrane since they are easily observable under an optical microscope and can be manipulated directly. They have also been studied to understand electric-field-induced deformation as well as fluid movement inside the vesicle [13].

Considering the varied functions and sizes of the biovesicles, continuous characterization of the membrane deformation under varying conditions is generally tedious and often very difficult to observe experimentally. Additionally, molecular interactions in smaller vesicles are affected by their membrane curvature which leads to uncertainties in experimental results [14]. Several analytical approaches have been presented to understand the fundamental physics of the membrane behavior [15–17]. However, due to the complex multiphysics nature of the problem, the analytical solutions often require restrictive assumptions. Sadik *et al.* presented a detailed theoretical analysis on the effects of using strong dc electric field on vesicles with different conductivities and compared their results with experimental observations [18]. However, the analytical model in their work, as well as the works of Hyuga *et al.* [16] are only valid for vesicles that are regular ellipsoids at the start and must maintain an ellipsoidal shape while they deform. Moreover, a number of hydrodynamic assumptions and simplifications are required for these analytical models in order to solve the governing equations. Numerical treatments of the problems have opened a wide window of opportunities in understanding these complex behaviors. Li *et al.* studied frequency dependence of membrane deformation in a nonuniform ac electric field [7]; MacQueen *et al.* investigated the change in elastic properties of cells due to electrodeformation using an effective dipole moment assumption [19]. However, most of these studies were either limited to the linear small deformation regime of the vesicles [18] or used the dipolar approximation that is not valid for deformed cells [20]. More recently, Hu *et al.* have presented detailed works on an algorithm development combining immersed interface and immersed boundary approaches for studying electrodeformation [21,22].

Despite the importance of these vesicles, a complete understanding of membrane behavior as well as fluid-structure interactions under electric fields is still lacking. In the present work, we investigate the electrodeformation dynamics of lipid vesicles under a wide range of applied dc electric fields. The vesicle membrane is represented as a massless immersed boundary. The bulk conductivity of the vesicle is adjusted accordingly to consider the heterogeneous electrical properties of the vesicle. The induced force of electric field is obtained using the Maxwell stress tensor approach. The effects of applied voltage, conductivity ratio, vesicle size, and initial aspect ratios on the electrodeformation dynamics are investigated in detail. The model is validated using several experimental results.

The rest of the paper is arranged as follows. In Sec. II, we present the mathematical model for a scenario where a vesicle is placed inside a microfluidic setup and subjected to a uniform applied electric potential difference. In Sec. III, we first compare experimental data with numerical
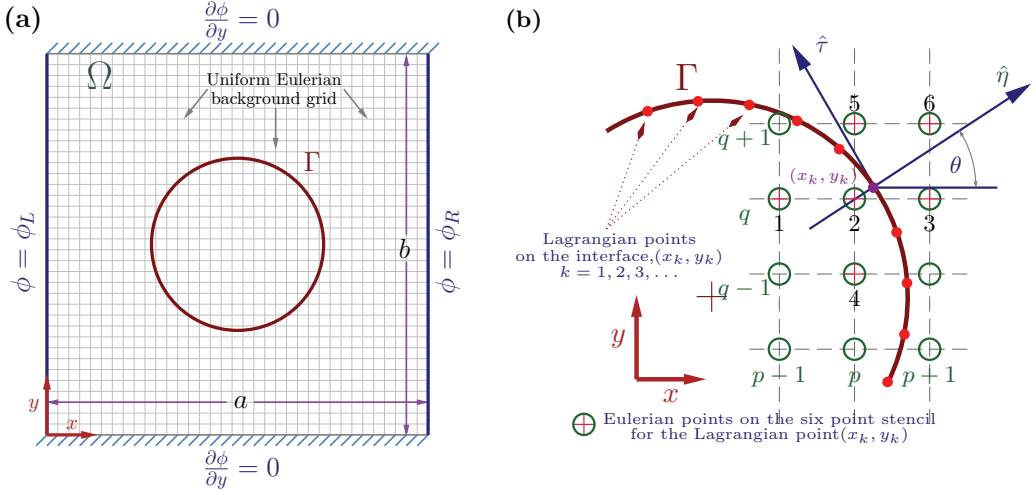
FIG. 1. Rectangular computational domain Ω used to model the vesicular microenvironment. (a) Boundary conditions for the electrostatic problems are shown. The vesicles in the domain have a finite size with membrane boundaries denoted by Γ. The undeformed circular vesicle has a radius of 10 μm while the domain dimensions are $a = b = 150$ μm. (b) Detail of the immersed boundary representation of the membrane. Vesicle membrane location in the regular Cartesian domain was calculated using spline interpolation [31].

results. Afterward, the effects of the magnitude of the applied field and the conductivity ratio on the deformation dynamics are observed. We also present the interaction of surrounding fluid media with deforming membrane and explore the electrodeformation phenomena for different initial vesicle aspect ratios.

II. MATHEMATICAL MODEL

We consider a physical scenario where a vesicle is submerged in an aqueous medium as shown in Fig. 1(a). This is similar to a biological cell suspended in buffer solution inside a microfluidic channel. The vesicle is subjected to a dc electric field. Here it is assumed that the vesicle is neutrally charged before the application of any external electric fields. Moreover, owing to a negligibly small electric double layer, electro-osmotic contributions can also be excluded [23]. Also, we do not consider van der Waals force since compared to electrostatic forces, the van der Waals and Brownian forces are negligible in these kinds of systems [24].

It is also assumed that the submerged aqueous medium is Newtonian with viscosity μ and density ρ. The electrical conductivity of the fluid outside the membrane is σ_{out} and that of the content inside is σ_{in}. When an electric field is applied through voltage difference on the left and right electrodes, the ensuing scenario can be described as a coupled electrostatic and fluid dynamic problem. In a microfluidic system, the advection and diffusion currents are much smaller than the drift current. Thus, for a dc electric field, the charge conservation equation can be simplified as

$$\nabla \cdot (\sigma \bar{E}) = 0. \tag{2.1}$$

The electric field ($\bar{E}$) is related to the electrical potential (ϕ) through

$$\bar{E} = -\nabla \phi. \tag{2.2}$$

Substituting Eq. (2.2) into the charge conservation equation, we arrive at the relation for the electric potential in the domain

$$\nabla \cdot (\sigma_{\text{in}} \nabla \phi_{\text{in}}) = 0, \quad \nabla \cdot (\sigma_{\text{out}} \nabla \phi_{\text{out}}) = 0, \tag{2.3}$$

where ϕ_{in} and ϕ_{out} are the potentials inside and outside the membrane. Imposing the jump in electric potential across the vesicle membrane and the continuity of normal current, we get the interface conditions on the membrane as

$$\varphi_{out}(x, y) - \varphi_{in}(x, y) = m(s), \tag{2.4}$$

$$\hat{\eta} \cdot \sigma_{out}\nabla\varphi_{out} - \hat{\eta} \cdot \sigma_{in}\nabla\varphi_{in} = n(s) = 0, \tag{2.5}$$

where $\hat{\eta}$ denotes the unit normal vector on the membrane, $m(s)$ and $n(s)$ are parametric representations of the jump conditions, and the parameter s tracks the material points of the interface. It must be noted that, every leaky dielectric, especially cell membranes, will act like a capacitor and have a finite charging time in an electric field. From Maxwell's equations, the characteristic time for electric phenomena is given by the ratio of dielectric permeability and conductivity of the membrane ($\varepsilon_{mem}\varepsilon_0/\sigma_{mem}$) [25], where ε_{mem} is the dielectric constant of the membrane, ε_0 is the vacuum permittivity, and σ_{mem} is the membrane conductance. Considering the membrane dielectric constant to be around 20 [26], and the conductivity on the order of 10^{-7} S/m [27], the characteristic time for electric phenomena is in the order of milliseconds. However, the capacitive charge buildup starts as soon as the lipid membranes are placed under an electric field leading to a voltage difference across it. Defining the transmembrane voltage V_{mem} as ($\phi_{in} - \phi_{out}$), the instantaneous membrane capacitive charging can be described by [22,28]

$$C_{mem}\frac{dV_{mem}}{dt} + G_{mem}V_{mem} = \hat{\eta} \cdot (\sigma_{in}\bar{E}_{in}) = \hat{\eta} \cdot (\sigma_{out}\bar{E}_{out}). \tag{2.6}$$

In Eq. (2.6), the membrane is modeled as a two-dimensional interface with effective capacitance $C_{mem} = \varepsilon_{mem}/h$ and conductance $G_{mem} = \sigma_{mem}/h$ where h is the membrane thickness.

Force density on the membrane due to this electrostatic interaction can be found from the Maxwell stress tensor $(\overline{\overline{M}})$ as

$$\bar{F}_{elec} = \nabla \cdot \overline{\overline{M}} = \nabla \cdot \varepsilon\left(\bar{E}\bar{E} - \frac{1}{2}|\bar{E}|^2\bar{I}\right), \tag{2.7}$$

where ε is the permittivity of the media where the force is being calculated and $\bar{I}$ is a unit tensor. The rectangular domain has two insulating boundaries at the bottom and top surfaces as shown in Fig. 1(a). Electrodes are placed on the left and right boundaries, where a prescribed potential is maintained to create an electric field. For simplicity, the vesicle is always placed at the geometric center of the domain, while the electrodes carry potentials of equal magnitude but opposite sign. The boundary conditions for the electric potential are presented in Table I.

The electric-field-driven viscous flow field can be described using the incompressible Navier-Stokes equations and continuity equation [29] as

$$\rho\left[\frac{\partial\bar{u}}{\partial t} + (\bar{u} \cdot \nabla)\bar{u}\right] = -\nabla p + \mu\nabla^2\bar{u} + \bar{B}_F(\bar{x}, t), \tag{2.8}$$

$$\nabla \cdot \bar{u} = 0. \tag{2.9}$$

TABLE I. Boundary conditions for the governing equation in the domain.

	Inlet ($x = 0$)	Outlet ($x = a$)	Bottom wall ($y = 0$)	Top wall ($y = b$)
Electrostatic Description	$\phi(x, y) = \phi_L$	$\phi(x, y) = \phi_R$	$\frac{\partial\phi(x,y)}{\partial y} = 0$	$\frac{\partial\phi(x,y)}{\partial y} = 0$
Fluid dynamic Description	Periodic	Periodic	$\hat{n} \cdot \bar{u} = 0; \hat{t} \cdot \bar{u} = 0$[a]	$\hat{n} \cdot \bar{u} = 0; \hat{t} \cdot \bar{u} = 0$[a]

[a]$\hat{n}$ and $\hat{t}$ are the unit normal and unit tangent vectors to the walls.

TABLE II. Geometric, mechanical, and electrical parameters used for the calculation of vesicle deformation.

Parameter	Value
Conductivity of the membrane, σ_{mem}	10^{-7} S/m [27]
Conductivity of the vesicle content, σ_{enc}	0.5 S/m [27]
Vesicle membrane thickness, h	5 nm
Vesicle radius, R	5–15 μm
Permittivity of the membrane, ε_{mem}	1.77×10^{-10} F/m [26]
Permittivity of the surrounding fluid medium, ε	7×10^{-10} F/m [20]
Density of the surrounding fluid medium, ρ	1000 kg/m^3
Viscosity of the surrounding fluid medium, μ	0.001 kg/(m s)

Here, $\bar{u}$ is the local velocity and $\bar{B}_F(\bar{x}, t)$ is the body force density acting on the fluid. This body force is a combination of the elastic forces in the membrane as well as the tensile or compressive forces arising from the applied electric field. In the fluid description, the domain is considered periodic in the horizontal direction which implies

$$\bar{u}(x = 0, y) = \bar{u}(x = a, y). \tag{2.10}$$

The top and bottom channel walls are assumed solid with no slip and no penetration boundary conditions as listed in Table I. All required geometric, mechanical, and electrical parameters as well as fluid properties are reported in Table II.

As shown in Figs. 1(a) and 1(b), the rectangular ($a \times b$) computational domain Ω is discretized with a uniform and fixed Eulerian grid. The immersed membrane boundary is outlined as Γ, where the interface is tracked in a Lagrangian manner with control points distributed on the membrane. Both immersed boundary and immersed interface descriptions represent the membrane in terms of localized force density formulations, where the interface is taken as one dimension smaller than the overall domain problem (e.g., one-dimensional interface for a two-dimensional domain) [30]. However, lipid vesicle membranes have a finite and often non-negligible thickness ($\sim$5–10 nm), and the properties of the membrane can be very different from the properties of the bulk fluid inside the vesicle. Therefore, the heterogeneous electrical characteristics of the vesicle, such as membrane electrical conductivity (σ_{mem}) and electrical conductivity of the fluid encapsulated by membrane (σ_{enc}) are replaced with an equivalent homogeneous conductivity, σ_{in} as [27,31]

$$\sigma_{\text{in}} = \sigma_{\text{mem}} \frac{2(1 - \beta)\, \sigma_{\text{mem}} + (1 + 2\beta)\, \sigma_{\text{enc}}}{(2 + \beta)\, \sigma_{\text{mem}} + (1 - \beta)\, \sigma_{\text{enc}}}; \quad \beta = \left(1 - \frac{h}{R}\right)^3, \tag{2.11}$$

where R is the radius of the vesicle. It should be mentioned that Eq. (2.11) is valid only when $h \ll R$, which is met by our description of the vesicle.

The elastic nature of the membrane as well as the fluid media outside and inside the membrane allow it to deform under an applied force. The magnitude of the applied force depends on vesicle shape as well as the electrical properties of the media inside and outside of the vesicle. To study these forces and their effects on surrounding fluids, we formulated a hybrid immersed interface-immersed boundary method. The solution methodology for the coupled electric and hydrodynamic system and details of the membrane mechanical models for deformation due to electric field are given in the Appendix.

III. DISCUSSION OF RESULTS

Before analyzing electrodeformation in a microfluidic system, the parameters need to be chosen accordingly so that the investigation is meaningful, and the results can be translated to understand broader physical phenomena. In this study, we first adjusted the stiffness parameter of the membrane
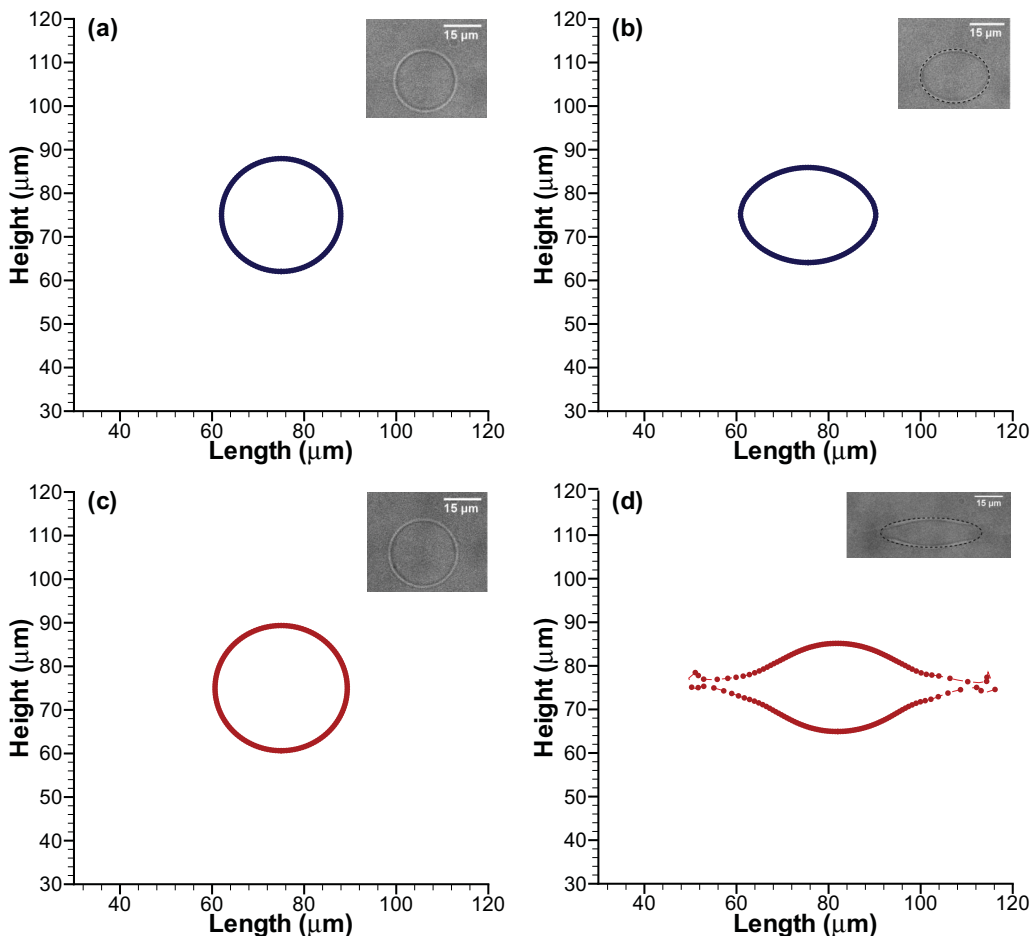
FIG. 2. Model result comparison with experimental data from Sadik *et al.* [18]. Vesicles are initially circular before application of an electric field in (a) and (c). (b) The deformation dynamics was tuned using experimental data after 500 μs at 0.9 kV/cm nominal applied field with conductivity ratio, $\lambda = 53$. (d) The tuned model captures vesicle deformation at higher applied voltage (1.5 kV/cm) and different conductivity ratio ($\lambda = 46.9$) as seen in the experiments [18].

to represent a lipid vesicle undergoing electrodeformation. Following experimental conditions from [18], first, a sample case was chosen where a vesicle of 26 μm initial diameter is exposed to a uniform electric field of 0.9 kV/cm. The conductivity ratio $\lambda = \sigma_{in}/\sigma_{out}$ was kept fixed at 53.0. Although the vesicle is initially circular, depending on the applied field, it generally takes an ellipsoidal shape after deformation. For the ease of discussion, we formally define the term aspect ratio, α, as the ratio of the ellipsoid axis along the horizontal (x axis) to the axis along the vertical (y axis). Thus, for a perfect sphere, $\alpha = 1.0$; it is greater than 1.0 for an oblate spheroid and less than 1 for a prolate one. After 500 μs, the experimental results show a deformation of the spherical vesicle ($\alpha = 1.0$) to an oblate spheroid ($\alpha = 1.31$), which is shown in Figs. 2(a) and 2(b) with corresponding numerical results found after adjusting the stiffness parameter. Next, using the same stiffness parameter, we studied a different case with a nominal applied field strength of 1.5 kV/cm and $\lambda = 46.9$. The initial diameter of the vesicle was 28.8 μm and after 500 μs, it was deformed into an oblate spheroid with $\alpha = 3.43$. Comparison with experimental data shows less than 4% difference as presented in Figs. 2(b) and 2(d). In this preliminary mechanical model
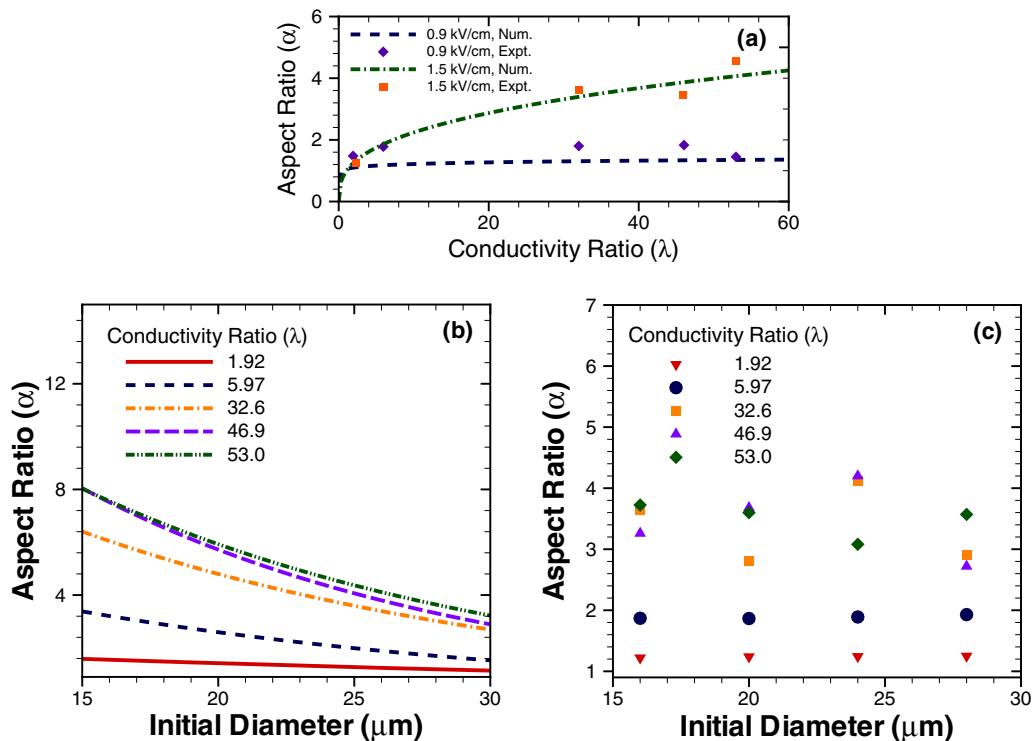
FIG. 3. Calculated aspect ratio (α), with respect to changing conductivity ratio (λ) for different applied potentials. Experimental results from [18] are included for comparison. The electric fields shown are nominal. (b) Change in aspect ratio after 500 μs for different conductivity ratios at 1.5 kV/cm nominal applied field corresponding to Sadik *et al.* [18] with the voltage jump across the membrane set to zero and the same scenario at (c) with voltage jump originating from membrane charging.

of the artificial vesicle membrane, we decided to use the simplest model that adequately captures the experimental findings. Unlike biological cells, the lipid vesicles used in the experiments do not have any underlying cytoskeleton. For that reason, the simple Hookean springs connecting each immersed boundary point to all other points yields satisfactory results over a wide range of applied voltage and conductivity ratios. For all the cases considered in our study, the 150 μm square domain is discretized with a 512×512 uniform spatial grid and the step size in time is 10 ns. A detailed convergence study of the numerical scheme, grid dependence, and error analysis with the chosen domain parameters has been presented in [20].

A. Effect of electric field magnitude and conductivity ratio

The extent of deformation of the flexible membrane with respect to the applied electric field is not a linear phenomenon. While comparing our model results, for validation with experimental data from [18] as presented in Fig. 3(a), we can observe a couple of distinct features. Firstly, the variation of aspect ratio (α) shows a rapid rise as the conductivity ratio (λ) is increased from 1. Later, it reaches a plateau for high λ values for a given applied electric field. Secondly, the effect of increasing electric field has a dramatic effect on the deformation dynamics, which we will discuss in Fig. 4 in detail. Theoretically, under some restrictive assumptions it has been shown that in the initial phase of increasing λ, the normal component of the Maxwell stress scales quadratically [18]. For larger values of λ, it converges to a constant value which explains the features in Fig. 3(a) where the normal component of the Maxwell stress is resulting in a horizontal pulling force on the vesicle
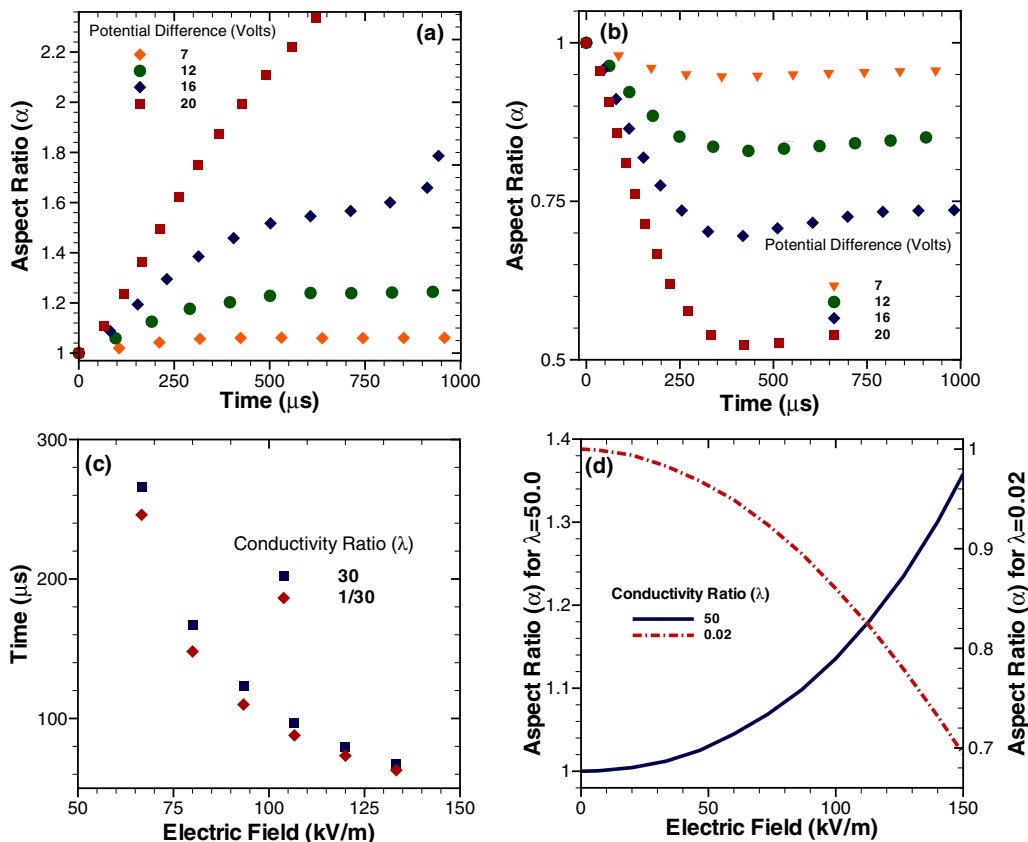
FIG. 4. Effect of the magnitude of applied potential difference with different conductivity ratios. Deformation of the vesicle in terms of the aspect ratio (α) with time for (a) conductivity ratio, $\lambda = 30$ and (b) $\lambda = 1/30$. (c) Starting from a perfect circle ($\alpha = 1$), the time required to reach $\alpha = 1.11$ for $\lambda = 30$ and $\alpha = 0.9$ for $\lambda = 1/30$. (d) Starting from $\alpha = 1$, the aspect ratios for both $\lambda > 1$ and $\lambda < 1$ at $125~\mu$s with increasing applied potential.

from both directions. Our model results capture the experimental trends for a wide range of λ and different levels of the applied electric field. It should be noted that, for higher levels of applied voltage, electroporation occurs very early in the experiments. In this study, we have not considered that regime. It should be mentioned that experimental evidence did not point to any conclusive effect of initial vesicle size on the deformation dynamics (Fig. 3 in [18]). However, their analytical model which did not consider any capacitive charging of the vesicle membrane showed clear dependence of the final aspect ratio on the vesicle size (Fig. 7 in [18]). In order to explore this scenario, we observed the deformations in our model under two different conditions. In the first case [Fig. 3(b)], the jump across the membrane is set to zero which corresponds to the analytical model in [18] while in the second case [Fig. 3(c)], we computed the voltage jump across the membrane. In the first case, our model predicts higher deformations for smaller vesicles. However, when membrane charging is considered, there was no clear relation between size and deformation. These results strongly indicate the induced charging behavior of the membrane under applied electric field.

Most of the experimental studies involving biomembranes are performed either in a buffer solution due to its chemical stability or in some other stable aqueous medium. In general, common buffer solutions have much higher (from 10 to 10 000 times higher) electrical conductivity compared to the biovesicles. However, in the case of artificial biomimetic vesicles, it is possible to alter the vesicle conductivity by altering the internal fluid media [18]. Therefore, it is possible to have a

wide range of experimental scenarios depending on the magnitude of conductivities of the media inside and outside the membrane. In order to compare our numerical results to the experimental observations from [18], we chose the conductivity ratio within the range of 1–50. It should be noted that this range physically corresponds to different concentrations of NaCl in aqueous solution as membrane-enclosed media and glucose solution as the surrounding media. For cases where the bulk conductivity of the vesicle is greater than the surrounding fluid, the conductivity ratio λ is fixed at 30, while for the opposite scenario, it is set at 1/30 in our model. Later, we also explore scenarios where λ itself is varying and discuss its implications. Several aspects of increasing the applied voltage on the electrodeformation are presented in Fig. 4. From a theoretical point of view, the electrostatic force obtained from the Maxwell stress tensor has a quadratic relation to the applied electric field as shown in Eq. (2.7). Analytic expansion of Eq. (2.7) for specific geometry has also shown this quadratic dependence [16]. This quadratic scaling is evident in Fig. 4(a) where $\lambda > 1$ and Fig. 4(b) where $\lambda < 1$. In both cases, a range of voltages was applied on the vesicle and the deformation in terms of α is presented against time. For deformation from circular (spherical) to oblate spheroids, α is greater than 1. For prolate spheroids, it is less than 1. The voltage range explored in our study is 7–20 V which corresponds to the nominal electric field strength of 46.667–133.33 kV/m. For cases with the weaker applied field, the vesicles show slow extension (compression) and they reach an apparent steady state. However, for cases with stronger fields, the behavior switches to a rapid deformation. The quadratic scaling is more apparent in Fig. 4(c) where we calculated the time taken by the vesicle to reach an aspect ratio of $\alpha = 1.1$ for $\lambda > 1$ or $\alpha = 0.9$ for $\lambda < 1$. Vesicles with an applied voltage lower than 7 V never get extended (or compressed) enough to reach this level. However, as the voltage is further increased, the time needed to reach the deformed shape decreases in a quadratic manner. Coupled with this observation, we studied the level of deformation after 125 μs under the whole range of applied field for $\lambda = 50$ and 1/50. The choice of time cutoff is influenced by the tendency of loss of integrity of the vesicle membrane under the applied nominal potential (20 V). As shown in Fig. 4(d), the applied field is a major factor in determining the extent of electrodeformation.

B. Effect of vesicle size

Theoretically, stress generated by the electric field, and hence the tensile or compressive forces acting on the boundary also shows dependence on the vesicle size. We varied the vesicle diameter from 10 to 30 μm and observed an almost linear increase in the initial force density with increasing size for a given applied voltage difference [Figs. 5(a) and 5(b)]. It should be noted that we considered the tensile force generated when $\lambda = 50$ in Fig. 5(a) to be positive. Consequently, for the case with $\lambda = 1/50$ shown in Fig. 5(b) the increasing compressive forces are more negative. The force vectors on the vesicles [shown as insets in Figs. 5(a) and 5(b)] also indicate this change in direction. However, the effect of vesicle size is not conclusive on the long-term deformation behavior of the vesicle as shown in Fig. 3(c) as well as in the experiments [18].

The contrast in electric field distribution between cases with $\lambda > 1$ and $\lambda < 1$ are presented in Fig. 6. In both cases, we start with a perfect circular shape ($\alpha = 1$). The vesicle deformations are shown in the electric field plots with field lines at $\alpha = 1.5$ for $\lambda = 30$ and $\alpha = 1/1.5$ for $\lambda = 1/30$. Also, in both cases, applied voltage at the left electrode is 10 V, while at the right electrode it is -10 volts. When the aqueous electrolyte media is subjected to a dc voltage gradient, ions in the fluid media start to migrate toward opposite electrodes. The ions inside the vesicles also get localized following the same principle. Thus, there is a buildup of opposite ions inside the vesicle (negative ions on the left side since the left electrode is the anode, and vice versa). However, since the fluid media outside is less conductive [Fig. 6(a)], the electric current cannot drive enough positive ions just outside the membrane to counter the buildup inside. As a result, a net negative charge accumulates around the left half of the vesicle with an equal amount of positive charge accumulating around the right half at the interface [32]. One critical point here is the timescale of this charge relaxation effect, which can be estimated from the electrical properties of the electrolyte in question.
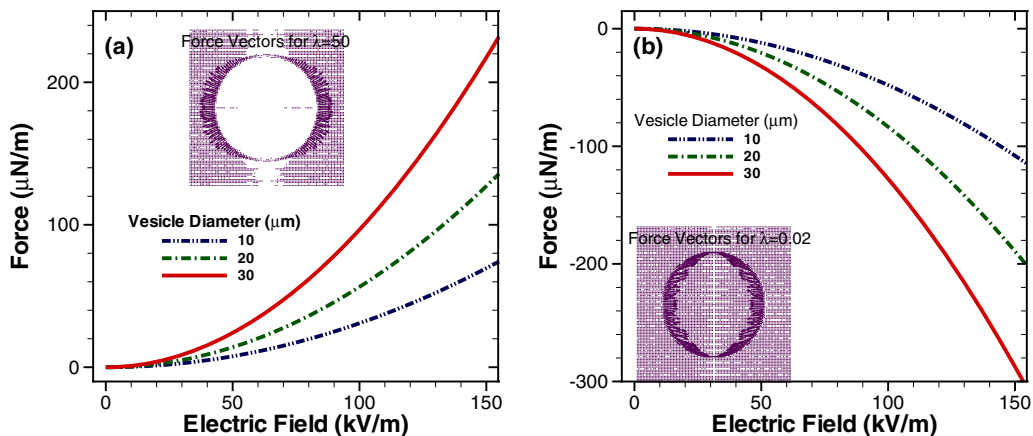
FIG. 5. Calculated force density on vesicles with different initial diameters. (a) Increase in force with increasing applied potential for $\lambda = 50$ and (b) $\lambda = 1/50$.

For the dilute aqueous media, this timescale is expressed as the ratio of the Debye screening length squared to the diffusivity of the electrolyte (ℓ_{Debye}^2/D). For aqueous solutions, the Debye screening length (ℓ_{Debye}) is between 1 and 100 nm, while the diffusivity (D) is on the order of $10^{-9}\,\text{m}^2/\text{s}$ [33]. This leads to rather fast bulk charge relaxation time which is on the order of nanoseconds. Consequently, the local changes in electric field are instantaneous, which further justifies the use of the steady-state governing equation [Eq. (2.1)] for electric potential.

Our numerical results indicate that the vesicle with an overall 30 times higher conductivity compared to the surrounding media behaves like a conductor with electric field lines entering and exiting the vesicle boundary as perpendicular lines [Figs. 6(a) and 6(b)]. As the ions at the inner side of the membrane dominate over the fluid medium ions on the interface, they experience a tensile pull toward the electrodes at the boundaries as shown in the force vector in Fig 5(a). The exact opposite scenario [Figs. 6(c) and 6(d)], with the fluid medium conductivity being 30 times higher than the vesicle results in the vesicle behaving like an insulator. In this case, there is an accumulation of net positive charge on the left half of the vesicle while an equal amount of net negative charge accumulates at the right half. For this reason, electric field lines are expelled from the surface. The corresponding electric-field-induced force is shown in Fig. 5(b). In this case, the force distribution is compressive in nature, i.e., vesicle experiences inward forces. In both cases, owing to the nature of the induced forces, the vesicle deforms continuously becoming an oblate ellipsoid for $\lambda > 1$ and a prolate one for $\lambda < 1$.

C. Electric-field-induced flow field

In most works with biovesicles, the surrounding flow patterns were ignored. However, for deformable vesicles, the fluid-solid interaction can produce interesting flow patterns. Two of these secondary flow patterns are shown as streamlines in Figs. 7(a) and 7(b), which are produced early in the transient deformation stage. Here, four vortices are created around the vesicle following bilateral symmetry with the major and minor axes of the spheroid as axes of symmetry. However, depending on the conductivity ratio, the vortices switch direction. When the vesicle is getting extended in the horizontal direction, the surrounding fluid layer follows it and generates vortices that follow the general direction of the force on the boundary to satisfy fluid continuity. The opposite is seen [Fig. 7(b)] in the case of compressive deformation where all four vortices switch direction. It should be noted that these flow patterns are resulting from a short but continuous deformation resulting from the dc electric field. When the electric field is removed, the vesicle would try to return to its
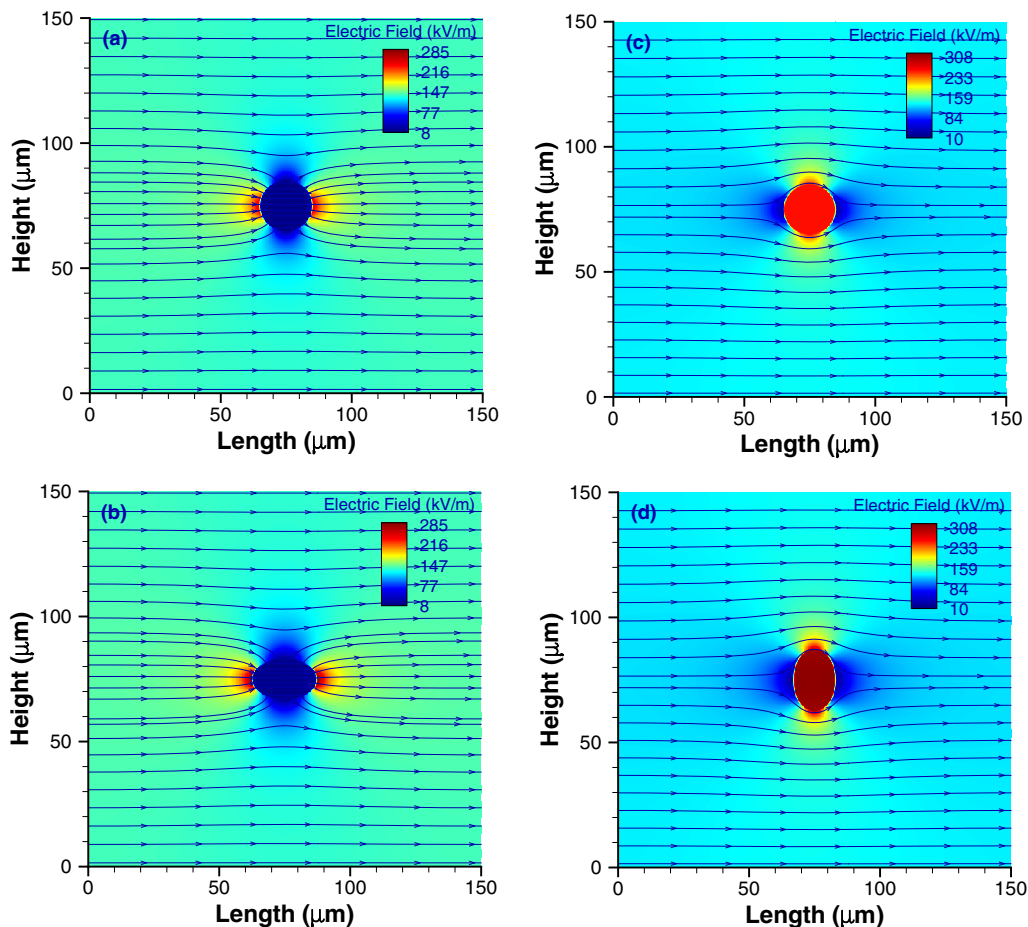
FIG. 6. Electric field distributions with field lines showing electrodeformation from spherical to prolate (oblate) spheroids with an applied potential difference of 20 V. (a), (b) Deformation from circular ($\alpha = 1$) to an oblate ellipse ($\alpha = 1.5$) for $\lambda = 30$. (c), (d) Deformation from circular to a prolate ellipse ($\alpha = 1/1.5$) for $\lambda = 1/30$.

resting undeformed state. That will reverse the flow directions in both cases. Similarly, in the case of an oscillatory pulsed dc field application, this reversal of local vortices can be used for microscale mixing applications. The velocity field, in that case, is very similar to that of immersed bubbles in streaming motion. In the future, we plan to see the fluid behavior for multiple vesicles with the same or different conductivities.

D. Effects of vesicle shape

All our simulations thus far began with an initially circular (spherical) vesicle. In general, the artificial vesicles or cells in experimental conditions have a wide range of initial aspect ratios. Here we compare the differences in the force dynamics for vesicles with several different initial aspect ratios. For this purpose, seven different initial aspect ratios were chosen ($\alpha = 1/3, 1/2, 1/1.5, 1.0, 1.5, 2.0, 3.0$) with $\lambda = 1/10$, $\lambda = 1/50$, and $\lambda = 1/100$, while a nominal applied field of 133.33 kV/m is used [Fig. 8(a)]. Since the vesicle is in equilibrium due to balancing forces on both the left and right half, here we present the integration of force density on the left half with all the results normalized by the maximum force (778 μN/m) at $\alpha = 1/3$ for $\lambda = 1/100$. As the
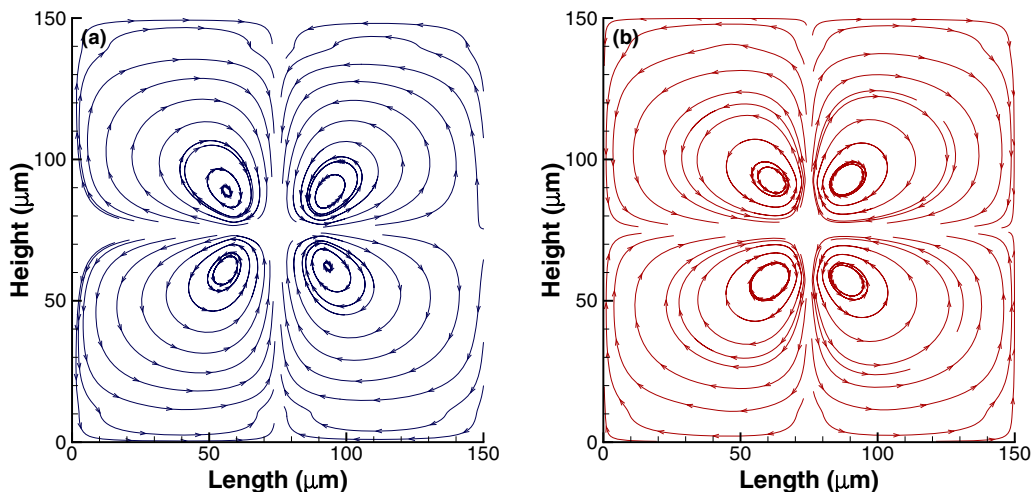
FIG. 7. Response of the surrounding fluid media due to the deformation of vesicles for an applied potential difference of 7 V. Streamlines for conductivity ratio (a) $\lambda = 50$ and (b) $\lambda = 1/50$. The four vortices switch directions in case (b) due to compressive force.

aspect ratio decreases from 1, the effective area for the horizontal compressive force increases. This results in the increased compressive force. However, with increasing aspect ratio, this trend tends to become flattened. A logical reasoning could be drawn based on the magnitude of the available area for each case by comparing it with the perfectly circular case. With lower aspect ratios ($\alpha < 1$), the compressive stress has a much higher normal surface to act upon. While in higher aspect ratios ($\alpha > 1$) the available surface area normal to the horizontal compressive force drops off relatively slowly, which explains the force approaching an asymptote. The time required to deform such a vesicle to an aspect ratio of $\alpha = 1/3$ consequently is smallest for the case with an initial aspect ratio $\alpha = 0.5$ and largest for an initial aspect ratio $\alpha = 2.0$, as shown in Fig. 8(b). The time required is
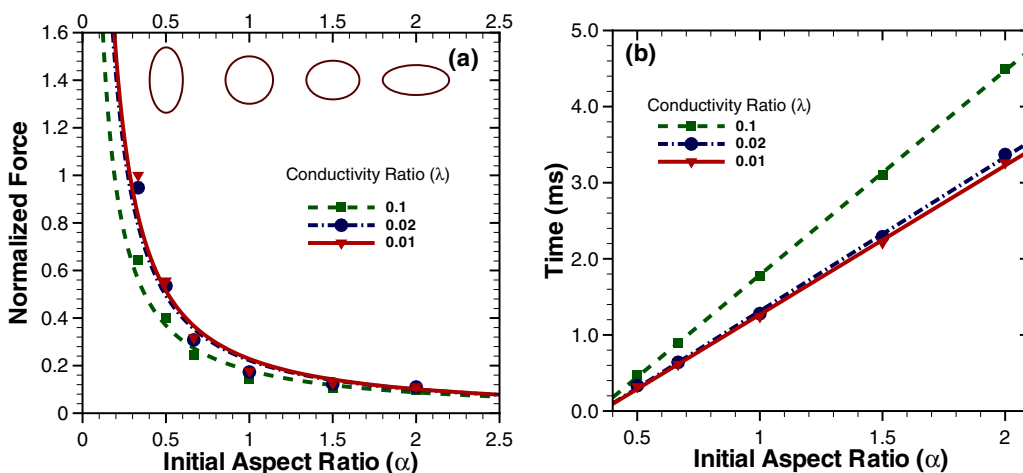

FIG. 8. (a) Effect of initial shape on the force experienced by the vesicle for different conductivity ratios with an applied potential difference of 20 V. (b) Time required to deform to an aspect ratio of $\alpha = 1/3$ for each case with the same applied voltage difference.

influenced by both the magnitude of the force and initial aspect ratio which controls the available normal surface for the force to act upon.

IV. CONCLUSIONS

In the studies of biovesicles like cell, virus, and artificial lipid vesicles, electric field application has become one of the most prominent manipulation techniques. Still, much remains unknown about the transient membrane deformation process due to electrostatic interactions arising from the differences in electrical properties of the media surrounding the membrane as well as membrane properties and cell configurations. Electrodeformation of flexible vesicles under a wide range of applied electric field has been studied in the present work. The electric field distribution was calculated using an immersed interface method, while the fluid-membrane interactions were obtained by solving the flow field using an immersed boundary approach. The membrane deformation dynamics under different electric fields and conductivity ratios were verified against experimental data. The numerical results show a number of transient deformation phenomena that are difficult to observe experimentally. Our study explores the transient deformation mechanisms which can help in the design of future experiments and assist in novel applications of electric-field-induced vesicle deformation.

Dependence on the electric field strength was clearly observed in our results. Numerical results demonstrated the scaling behavior of the applied force arising from the electric field, which were substantiated with analytical results. Our study also pointed out the relative levels of force experienced by vesicles of different initial shapes. We plan to explore the implications of the initial membrane shape on a number of parameters such as stiffness and bending rigidity in a future work.

Interesting fluid behavior was observed around the deforming vesicle that also showed variation based on the change in conductivity ratio. Vortices created by these deforming vesicles can be used for mixing in microchannels. Also, an extension of the current model to a three-dimensional description of the vesicle will help to provide further insight into the discrepancies between current experimental and numerical studies.

ACKNOWLEDGMENTS

APPENDIX

1. Numerical model and methods

The coupled hydrodynamic and electric system is solved using a hybrid immersed boundary and immersed interface technique. Both these methods employ a non-body-fitted Cartesian gridding approach in discretizing the physical domain (Fig. 1). This is computationally advantageous due to almost no cost for grid generation. However, for the grid points near the membrane interface, which are much smaller in number compared to regular grid points, special treatment is required. In the immersed boundary method, the localized variables (e.g., force and velocity) on the membrane are interpolated to nearby grid point using an approximate delta function. The immersed interface approach avoids the smearing by altering the discretized equations near the interface. Due to the inherent numerical accuracy and stability, the immersed interface method is very well suited for the elliptic electromagnetic interface problem [34]. The immersed boundary method, on the contrary, is appropriate for the fluid-structure interaction problem encountered in the electrodeformation of the immersed biological membranes [35,36]. Previously, we have combined the immersed interface and the immersed boundary methods to study particle-particle dielectrophoretic and electrophoretic interactions [20,24]. Recently, a similar numerical approach was taken by Hu *et al.* to further develop

the algorithm for electrodeformation problems [21,22]. Although the underlying numerical methods are the same for both their and our works, there are differences in the implementations of both immersed interface and immersed boundary methods. For example, treatment of jump conditions, the membrane dynamics, localization, and spreading of membrane forces are approached differently in each study. The specific details of the numerical method pertinent to the electrodeformation problem are presented below.

The electrostatic problem [Eqs. (2.1)–(2.5)] at a given instant is independent of the fluid description and hence, is solved directly by the immersed interface technique by first transforming it to an equivalent elliptic problem with piecewise constant conductivity and modified interface conditions. Here, the governing equations and the jump conditions are modified as

$$\nabla^2 \phi_{r,\text{out}} + \frac{\nabla \sigma_{\text{out}}}{\sigma_{\text{out}}} \cdot \nabla \phi_{r,\text{out}} = 0, \tag{A1}$$

$$\nabla^2 \phi_{r,\text{in}} + \frac{\nabla \sigma_{\text{in}}}{\sigma_{\text{in}}} \cdot \nabla \phi_{r,\text{in}} = 0. \tag{A2}$$

$$\phi_{r,\text{out}}(x, y) - \phi_{r,\text{in}}(x, y) = m(s), \tag{A3}$$

$$\hat{\eta} \cdot \nabla \varphi_{r,\text{out}} - \hat{\eta} \cdot \nabla \varphi_{r,\text{in}} = r(s), \tag{A4}$$

where $\phi_r(x, y)$ is a solution set of the modified problem taken as a function of $r(s)$. The instantaneous solution of the equation for capacitive charging (Eq. 2.6) at each immersed interface point yields the transmembrane potential which is used to calculate the voltage jump across the membrane in Eq. (A3). Now, if we consider $\phi^*(x, y)$ as a solution to the original problem [Eqs. (2.1)–(2.5)] and define $r^*(s) = \hat{\eta} \cdot \nabla \varphi^*_{\text{out}} - \hat{\eta} \cdot \nabla \varphi^*_{\text{in}}$, then it can be shown that $\phi^*(x, y)$ also satisfies the modified problem and jump conditions, thus $r(s) \equiv r^*$ [34]. Which implies $\varphi_{r*}(x, y) \equiv \varphi^*(x, y)$ and

$$\hat{\eta} \cdot \sigma_{\text{out}} \nabla \varphi_{r*,\text{out}} - \hat{\eta} \cdot \sigma_{\text{in}} \nabla \varphi_{r*,\text{in}} = n(s). \tag{A5}$$

Thus, the original problem is solved by finding $r(s)$ through r^* and $\phi_{r*}(x, y)$ from the solution of the modified problem. The assumption of piecewise constant conductivity makes the modified description [Eqs. (A1)–(A4)] a Poisson problem which can be solved by fast solvers. With h being the uniform mesh size in the Cartesian grid, and n_x and n_y as the number of grid points in the coordinate directions, the modified governing equation can be written in the discrete form for any arbitrary grid point inside the domain (p, q) as

$$\frac{1}{h^2}(\Phi_{p+1,q} + \Phi_{p-1,q} + \Phi_{p,q+1} + \Phi_{p,q-1} - 4\Phi_{p,q}) = C_{pq},$$
$$\text{where} \quad 1 \leqslant p \leqslant n_x - 1; \quad 1 \leqslant q \leqslant n_y - 1. \tag{A6}$$

Here the correction term C_{pq} on the right side is zero everywhere except at the grid points, where the interface cuts through the five-point stencil [points 2, 3, and 5 in Fig. 1(b)]. In a compact matrix-vector form, Eq. (A6) can be written as

$$A\Phi + BR = \Theta, \tag{A7}$$

where A and B are coefficient matrices for the solution Φ, R is the discrete form of the modified interface jump condition r^*, and Θ is a vector. The correction term C_{pq} is also mapped into BR in Eq. (A7). Since $\phi^*(x, y)$ satisfies the discrete form of Eq. (2.5), and the solutions inside and outside the interface depend linearly on Φ and R [34], we get the final equation as

$$K\Phi + ER = \Xi, \tag{A8}$$

where K and E are coefficient matrices and Ξ is a vector. The linear systems of equations are combined by eliminating Φ using $G = (E - KA^{-1}B)$ and $H = (\Xi - KA^{-1}\Theta)$ which gives

$$GR = H. \tag{A9}$$

Equation (A9) is solved for R using a GMRES routine with a weighted least-squared interpolation scheme [37]. Finally, with the knowledge of R, the discretized system of equations is solved iteratively through successive calls to the PARDISO solver [38]. Further details on the formulation of the hybrid method, convergence, grid refinement, and accuracy can be found in [20,24].

Once the electric potential from the electrostatic equations are found, we can calculate the body force term $[\bar{B}_F(\bar{x}, t)]$ in Eq. (2.8), which is then supplied to the fluid flow equations. In order to solve Eqs. (2.8) and (2.9) using the immersed boundary approach, we assume the elastic immersed membrane to be neutrally buoyant. Based on this assumption, the membrane boundary Γ can be expressed as singular force density contributions in the body force term in Eq. (2.8) following the immersed boundary approach as [39]

$$\bar{F}_{\text{IB}}(\bar{x}, t) = \int_{\Gamma} \bar{f}_{\text{elastic}}(s, t)\delta[\bar{x} - \bar{X}(s, t)]ds. \tag{A10}$$

Here, $\bar{F}_{\text{IB}}(\bar{x}, t)$ is the Eulerian force density acting on the fluid, while $\bar{f}_{\text{elastic}}(s, t)$ is the Lagrangian boundary force density with respect to ds. In Eq. (A10), $\delta(\bar{x})$ is a two-dimensional Dirac delta function which ensures the mathematical representation of the physical membrane as body force terms in the two-dimensional domain as required at a given time [20]. Although $\bar{F}_{\text{IB}}(\bar{x}, t)$ is singular on the immersed boundary, we note that in the numerical method we use a regularized delta function such that the force density at the immersed boundary is well defined. This integral over the delta function provides the resulting force exerted by the section of the immersed boundary on the fluid in that control volume [40]. On the right side of Eq. (A10), the term $\bar{X}(s, t)$ represents the massless immersed boundary as a simple closed curve of length L with $\bar{X}(0, t) = \bar{X}(L, t)$ and $0 \leqslant s \leqslant L$. The parameter s tracks the material points of the boundary which is carried along with the fluid by the local fluid velocity $\bar{u}(\bar{x}, t)$ as

$$\frac{\partial \bar{X}(s, t)}{\partial t} = \bar{U}[\bar{X}(s, t), t] = \int_{\Omega} \bar{u}(\bar{x}, t)\delta[\bar{x} - \bar{X}(s, t)]d\bar{x}. \tag{A11}$$

The Eulerian forces due to the applied electric field ($\bar{F}_{\text{elec}}$) from Eq. (2.7) are interpolated on the Lagrangian immersed boundary points and added to the elastic force density ($\bar{F}_{\text{IB}}$) to compute the total body force on the membrane. Further details on the specific delta function and the numerical integration have been discussed in detail in [24].

The Lagrangian force density $\bar{f}_{\text{elastic}}(s, t)$ can be generated from the combination of elastic stretching, bending, or stiff tethering of the immersed boundary. For our previous works on dielectrophoresis with rigid particles [20,24], we considered each immersed boundary point on the interface to be connected to all other points on that immersed boundary through elastic links which obey a generalized Hooke's law following

$$\bar{f}_{\text{elastic}}(s, t) = \bar{S}[\bar{X}(s, t), t]. \tag{A12}$$

The aforementioned equation describes the boundary force density at time t in terms of the boundary configuration at that time. The function $\bar{S}$ satisfies the generalized Hooke's law [24]. For example, considering two arbitrary immersed boundary points i and j, the force $\bar{f}_{\text{elastic}}^{ij}$ due to the elastic link between the two points can be obtained by

$$\bar{f}_{\text{elastic}}^{ij} = \kappa\left(\|\bar{X}_j - \bar{X}_i\| - L_{ij}^0\right)\frac{\bar{X}_j - \bar{X}_i}{\|\bar{X}_j - \bar{X}_i\|}, \tag{A13}$$

where κ is the stiffness parameter of the link and L_{ij}^0 is the initial resting length of the link. As the membrane deforms due to the applied field, its initial resting position is altered resulting in the

generation of elastic forces. Consequently, these body forces alter the flow field surrounding the membrane. Therefore, after solving the electric field, discretized forms of Eqs. (2.8) and (2.9) are solved using fast-Fourier transform (FFT) [41]. The discrete forms are given as

$$\rho \left\{ \frac{(\bar{u}^{n_t+1} - \bar{u}^{n_t})}{\Delta t} + \sum_{\xi=x,y} \left[\left(u_\xi^{n_t} D_\xi^\pm \right) \bar{u}^{n_t} \right] \right\} = -\bar{D}^0 p^{n_t+1} + \mu \sum_{\xi=x,y} [(D_\xi^+ D_\xi^-)\bar{u}^{n_t+1}] + \bar{B}_F^{n_t}, \quad \text{(A14)}$$

$$\bar{D}^0 \cdot \bar{u}^{n_t+1} = 0, \quad \text{(A15)}$$

where D^+, D^-, and D^0 are the forward, backward, and central spatial difference operators, $u_\xi^{n_t} D_\xi^\pm$ and $\bar{D}^0$ are the upwind and gradient difference operators, respectively, as defined in [40]. From the flow-field solution, local velocities of the immersed boundary points are updated using the discrete form of Eq. (A10). It should be mentioned that, owing to the very low Reynolds number in the microfluidic channel, solving only the Stokes equations might have been enough. However, numerical implementation of the solution procedure of time-dependent Stokes flow using an immersed boundary method with periodic boundaries does not offer significant computational advantage over solving the full Navier-Stokes equations. Moreover, we are using fast-Fourier transform based Navier-Stokes solvers which have been shown to perform very well at low Reynolds numbers [42].

---

[1] A. Arakelyan, W. Fitzgerald, S. Zicari, C. Vanpouille, and L. Margolis, Extracellular vesicles carry HIV Env and facilitate HIV infection of human lymphoid tissue, Sci. Rep. **7**, 1695 (2017).

[2] R. Molinaro, C. Corbo, J. O. Martinez, F. Taraballi, M. Evangelopoulos, S. Minardi, I. K. Yazdi, P. Zhao, E. De Rosa, M. B. Sherman, A. De Vita, N. E. T. Furman, X. Wang, A. Parodi, and E. Tasciotti, Biomimetic proteolipid vesicles for targeting inflamed tissues, Nat. Mater. **15**, 1037 (2016).

[3] B. Yang, X. Dong, Q. Lei, R. X. Zhuo, J. Feng, and X. Z. Zhang, Host-guest interaction-based self-engineering of nano-sized vesicles for co-delivery of genes and anticancer drugs, ACS Appl. Mater. Interfaces **7**, 22084 (2015).

[4] M. W. Rezanoor and P. Dutta, Combined AC electroosmosis and dielectrophoresis for controlled rotation of microparticles, Biomicrofluidics **10**, 024101 (2016).

[5] R. Dimova, N. Bezlyepkina, M. D. Jordö, R. L. Knorr, K. A. Riske, M. Staykova, P. M. Vlahovska, T. Yamamoto, P. Yang, and R. Lipowsky, Vesicles in electric fields: Some novel aspects of membrane behavior, Soft Matter **5**, 3201 (2009).

[6] R. Dimova and K. A. Riske, in *Handbook of Electroporation*, edited by Damijan Miklavčič (Springer, Cham, 2017), p. 235.

[7] H. Li, T. Ye, and K. Y. Lam, Qualitative and quantitative analysis of dynamic deformation of a cell in nonuniform alternating electric field, J. Appl. Phys. **110**, 104701 (2011).

[8] S. Kakorin, T. Liese, and E. Neumann, Membrane curvature and high-field electroporation of lipid bilayer vesicles, J. Phys. Chem. B **107**, 10243 (2003).

[9] T. Z. Jubery, S. K. Srivastava, and P. Dutta, Dielectrophoretic separation of bioparticles in microdevices: A review, Electrophoresis **35**, 691 (2014).

[10] Y. Teng, M. S. Pang, J. Y. Huang, and C. Y. Xiong, Mechanical characterization of cancer cells during TGF-β1-induced epithelial-mesenchymal transition using an electrodeformation-based microchip, Sens. Actuators, B **240**, 158 (2017).

[11] E. Du, M. Dao, and S. Suresh, Quantitative biomechanics of healthy and diseased human red blood cells using dielectrophoresis in a microfluidic system, Extreme Mechan. Lett. **1**, 35 (2014).

[12] K. A. Riske, N. Bezlyepkina, R. Lipowsky, and R. Dimova, Electrofusion of model lipid membranes viewed with high temporal resolution, Biophys. Rev. Lett. **1**, 387 (2006).

[13] P. M. Vlahovska, R. S. Gracia, S. Aranda-Espinoza, and R. Dimova, Electrohydrodynamic model of vesicle deformation in aternating electric fields, Biophys. J. **96**, 4789 (2009).

[14] R. Dimova, S. Aranda, N. Bezlyepkina, V. Nikolov, K. A. Riske, and R. Lipowsky, A practical guide to giant vesicles. Probing the membrane nanoregime via optical microscopy, J. Phys.: Condens Matter **18**, S1151 (2006).

[15] M. Winterhalter and W. Helfrich, Deformation of spherical vesicles by electric-fields, J. Colloid Interface Sci. **122**, 583 (1988).

[16] H. Hyuga, K. Kinosita, and N. Wakabayashi, Deformation of vesicles under the influence of strong electric-fields, Jpn. J. Appl. Phys. **30**, 1141 (1991).

[17] T. Yamamoto, S. Aranda-Espinoza, R. Dimova, and R. Lipowsky, Stability of spherical vesicles in electric fields, Langmuir **26**, 12390 (2010).

[18] M. M. Sadik, J. B. Li, J. W. Shan, D. I. Shreiber, and H. Lin, Vesicle deformation and poration under strong dc electric fields, Phys. Rev. E **83**, 066316 (2011).

[19] L. A. MacQueen, M. D. Buschmann, and M. R. Wertheimer, Mechanical properties of mammalian cells in suspension measured by electro-deformation, J. Micromech. Microeng. **20**, 065007 (2010).

[20] M. R. Hossan, R. Dillon, and P. Dutta, Hybrid immersed interface-immersed boundary methods for AC dielectrophoresis, J. Comput. Phys. **270**, 640 (2014).

[21] W. F. Hu, M. C. Lai, and Y. N. Young, A hybrid immersed boundary and immersed interface method for electrohydrodynamic simulations, J. Comput. Phys. **282**, 47 (2015).

[22] W. F. Hu, M. C. Lai, Y. Seol, and Y. N. Young, Vesicle electrohydrodynamic simulations by coupling immersed boundary and immersed interface method, J. Comput. Phys. **317**, 66 (2016).

[23] Y. Ai and S. Z. Qian, DC dielectrophoretic particle-particle interactions and their relative motions, J. Colloid Interface Sci. **346**, 448 (2010).

[24] M. R. Hossan, R. Dillon, A. K. Roy, and P. Dutta, Modeling and simulation of dielectrophoretic particle-particle interactions and assembly, J. Colloid Interface Sci. **394**, 619 (2013).

[25] D. A. Saville, Electrohydrodynamics: The Taylor-Melcher leaky dielectric model, Annu. Rev. Fluid Mech. **29**, 27 (1997).

[26] P. Tian, Computational protein design, from single domain soluble proteins to membrane proteins, Chem. Soc. Rev. **39**, 2071 (2010).

[27] M. Pavlin and D. Miklavcic, Effective conductivity of a suspension of permeabilized cells: A theoretical analysis, Biophys. J. **85**, 719 (2003).

[28] J. Seiwert, M. J. Miksis, and P. M. Vlahovska, Stability of biomimetic membranes in DC electric fields, J. Fluid Mech. **706**, 58 (2012).

[29] P. Dutta, A. Beskok, and T. C. Warburton, Numerical simulation of mixed electroosmotic/pressure driven microflows, Numer. Heat Transfer, Part A **41**, 131 (2002).

[30] Z. Li and K. Ito, *The Immersed Interface Method: Numerical Solutions of PDEs Involving Interfaces and Irregular Domains* (SIAM, Pennsylvania, 2006).

[31] V. H. Pauly and H. Schwan, Über die impedanz einer suspension von kugelförmigen teilchen mit einer schale, Z. Naturforsch., B: J. Chem. Sci. **14**, 125 (1959).

[32] R. Hossan Mohammad, D. Dutta, N. Islam, and P. Dutta, Review: Electric field driven pumping in microfluidic device, Electrophoresis **39**, 702 (2018).

[33] M. Z. Bazant, K. Thornton, and A. Ajdari, Diffuse-charge dynamics in electrochemical systems, Phys. Rev. E **70**, 021506 (2004).

[34] Z. Li, A fast iterative algorithm for elliptic interface problems, SIAM J. Num. Anal. **35**, 230 (1998).

[35] C. S. Peskin, Numerical analysis of blood flow in the heart, J. Comput. Phys. **25**, 220 (1977).

[36] P. Bagchi, Mesoscale simulation of blood flow in small vessels, Biophys. J. **92**, 1858 (2007).

[37] Y. Saad and M. H. Schultz, GMRES: A generalized minimal residual algorithm for solving nonsymmetric linear-systems, SIAM J. Sci. Stat. Comput. **7**, 856 (1986).

[38] O. Schenk and K. Gartner, On fast factorization pivoting methods for sparse symmetric indefinite systems, Electron. Trans. Num. Anal. **23**, 158 (2006).

[39] C. S. Peskin, The immersed boundary method, Acta Numerica **11**, 479 (2002).

[40] M. C. Lai and C. S. Peskin, An immersed boundary method with formal second-order accuracy and reduced numerical viscosity, J. Comput. Phys. **160**, 705 (2000).

[41] C. Y. Hsu and R. Dillon, A 3D motile rod-shaped monotrichous bacterial model, Bull. Math. Biol. **71**, 1228 (2009).

[42] C. S. Peskin and D. M. McQueen, in *Case Studies in Mathematical Modeling — Ecology, Physiology, and Cell Biology*, edited by H. G. Othmer, F. R. Adler, M. A. Lewis, and J. C. Dallon (Prentice-Hall, New Jersey, 1997), p. 309.